APPLIED SCIENCES AND ENGINEERING

Design and function of biomimetic multilayer water purification membranes

Shengjie Ling,[1,2]* Zhao Qin,[1]* Wenwen Huang,[2] Sufeng Cao,[3] David L. Kaplan,[2]† Markus J. Buehler[1,4,5]†

Multilayer architectures in water purification membranes enable increased water throughput, high filter efficiency, and high molecular loading capacity. However, the preparation of membranes with well-organized multilayer structures, starting from the nanoscale to maximize filtration efficiency, remains a challenge. We report a complete strategy to fully realize a novel biomaterial-based multilayer nanoporous membrane via the integration of computational simulation and experimental fabrication. Our comparative computational simulations, based on coarse-grained models of protein nanofibrils and mineral plates, reveal that the multilayer structure can only form with weak interactions between nanofibrils and mineral plates. We demonstrate experimentally that silk nanofibril (SNF) and hydroxyapatite (HAP) can be used to fabricate highly ordered multilayer membranes with nanoporous features by combining protein self-assembly and in situ biomineralization. The production is optimized to be a simple and highly repeatable process that does not require sophisticated equipment and is suitable for scaled production of low-cost water purification membranes. These membranes not only show ultrafast water penetration but also exhibit broad utility and high efficiency of removal and even reuse (in some cases) of contaminants, including heavy metal ions, dyes, proteins, and other nanoparticles in water. Our biomimetic design and synthesis of these functional SNF/HAP materials have established a paradigm that could lead to the large-scale, low-cost production of multilayer materials with broad spectrum and efficiency for water purification, with applications in wastewater treatment, biomedicine, food industry, and the life sciences.

INTRODUCTION

Membranes for water treatment have progressively been developed in recent years to address global challenges of water pollution, because they are an energy- and waste-efficient means to remove molecular-level contaminants (1–3). A variety of new materials [for example, polymers (4–8), biopolymers (9–12), and inorganic nanomaterials (13–23)] and novel fabrication methods [for example, block copolymer self-assembly (5, 6, 8), template synthesis (7, 15), track-etching technique (23, 24), chemical vapor deposition (25, 26), and layer-by-layer assembly (27)] have been developed to improve the purification efficiency of these membranes. However, preparing low-cost water purification membranes while retaining mechanical strength and high purification performance remains a challenge.

Multilayer filtration membranes have several unique advantages to solve this problem, including enhanced throughput, high filter efficiency, high molecular loading capacity, and low pressure drop (22, 28–32). Nature has used multilayer architectures for water purification for millions of years in environments that consist of vegetation, gravel, sand, and soil layers (33). When rainfall lands in forests, deserts, and wetlands, the water soaks into the ground through the vegetation layer, where large soil particles are trapped by the gravel layer and the rainfall is further cleansed through fine layers of sand and soil (soil horizons). However, directly mimicking the design and ingenuity of nature in the laboratory for practical applications remains

a challenge. Layer-by-layer assembly is one method of building multilayer structures (34–36), but this approach comes with several drawbacks, such as limited material selectivity, a time-consuming and tedious process, and the relatively weak mechanical properties of the resultant membranes. Recently, a variety of laminar inorganic nanosheets, such as graphene oxide (16–19), molybdenum disulfide (20), and tungsten disulfide (21), have been used to build layered purification membranes. However, without complex and expensive processing, these membranes will not have nanosized porous structures. Water can only permeate from gaps and interlayer spaces between nanosheets; thus, their permeation rate leaves significant room for improvement.

Besides laminar inorganic nanomaterials, biomaterials (for example, cellulose, chitin, and proteins) have also been used to make filtration membranes (9–11). Recently, we have shown that liquid-exfoliated silk nanofibrils (SNFs) could be used to make filtration membranes with high water flux and efficient separation performance for dyes, proteins, and nanoparticles (11). However, the pristine SNF membrane, similar to other biomaterial-based filtration systems, has small and untunable pore sizes (for example, diameters of 8 to 12 nm in the liquid-exfoliated SNF membrane). Thus, water (and solvent) permeation rates decline markedly with an increase of membrane thickness, and the molecular loading capacity for purification is also limited. This problem can be solved, to some extent, by combining different protein fibrils within the same membrane. For instance, we can integrate SNFs and amyloid fibrils into a homogeneous membrane (37) and enzymatically etch amyloids from mature hybrid membranes, resulting in tunable nanoporous structures. However, the stability and mechanical properties of the resultant membranes require improvement, especially for the membranes with a high percentage of amyloids, as well as those that have been enzymatically etched. Although biomaterials have imperfections, they have been shown to be a useful option for developing novel water treatment membranes, in part because of their cost-saving, environmentally friendly, and biocompatibility advantages. However, it remains a

[1]Department of Civil and Environmental Engineering, Massachusetts Institute of Technology, 77 Massachusetts Avenue, Cambridge, MA 02139, USA. [2]Department of Biomedical Engineering, Tufts University, Medford, MA 02155, USA. [3]Department of Chemical and Biological Engineering, Tufts University, Medford, MA 02155, USA. [4]Center for Materials Science and Engineering, Massachusetts Institute of Technology, Cambridge, MA 02139, USA. [5]Center for Computational Engineering, Massachusetts Institute of Technology, Cambridge, MA 02139, USA.
*These authors contributed equally to this work.
†Corresponding author. Email: david.kaplan@tufts.edu (D.L.K.); mbuehler@mit.edu (M.J.B.)

challenge to efficiently and accurately produce multilayer porous structures of biomaterials to achieve optimized separation performance, mechanical resilience, and stability. This limitation is due to the challenges of materials design, which require an in-depth understanding of both the molecular interactions and chemical processes.

Here, we design a de novo strategy to make multilayer nanoporous membranes via the integration of computational simulation and experimental fabrication. The core methodology is to use soft and hard nanobuilding blocks for the construction of multilayer nanoporous structures. The soft layer, which has a smaller pore size (several nanometers in diameter), serves as a size selectivity layer to effectively filter out molecular-level contaminants. The hard layer, which has a large pore size and high porosity, allows water to pass through quickly and provides structural support for the soft layer. In addition, the alternating arrangement of these two layers can further improve the permeability of these membranes. Many natural systems, such as nacre, enamel, and bone, use proteins and calcium-based minerals to build their sophisticated multilayer architectures with enhanced physical properties (38). Moreover, both proteins and calcium-based minerals have shown promising applications in water purification and other extensive fields (39, 40); thus, we selected these two components as starting building blocks to generate the composites.

RESULTS

To identify the conditions where these two components can form porous multilayer structures, we developed coarse-grained models of the protein nanofibrils (NFs) and calcium-based mineral nanoplates (NPs). Each NF and NP was modeled by an elastic network with care-fully chosen elastic constants to reflect the elastic properties of the materials and with mass concentrated at the junction beads to reflect the material densities (see section S2). Using the collection of these models, we ran molecular dynamics (MD) simulations to simulate their assembly during the deposition process in water flow. Figure 1 shows a comparison of the assembly process of SNFs and hydroxyapatite (HAP) nanocrystals, which demonstrates that, by tuning the material stiffness, density, and interfacial interactions between the subunits, the SNFs and HAP nanocrystals can assemble to form either a multilayer structure with a clear boundary between two material phases or a homogeneous mixture of the two materials. We discovered that, for a wide range of mineral density (as the material density of the protein is almost fixed) and stiffness of NFs and NPs, the interfacial energy (γ) between NF and NP plays the dominant role in governing the assembly. The computational simulations for weak NF/NP interaction revealed that the NFs are assembled into a continuous network during the deposition process and that their deposition rates are smaller than those of NP flakes that lack this self-assembly process. Turning to strong NF/NP interactions, NF and NP flakes are well mixed by self-assembly before they are deposited on the substrate. Accordingly, an NF/NP interaction weaker than both NF/NF and NP/NP interactions ($\gamma < 0.217$ J/m^2, the average surface energy measured for protein filament assembly; see section S2) is necessary to form the layered structures (Fig. 1 and movies S1 to S3). This finding is critical for selecting a suitable combination of materials to form multilayer structures, because many protein/mineral combinations have strong interfacial interactions and are not suitable for use as raw materials to form these multilayer structures.

On the basis of these simulations, different material combinations were scanned, and SNFs and HAP were selected to conduct the experiments.
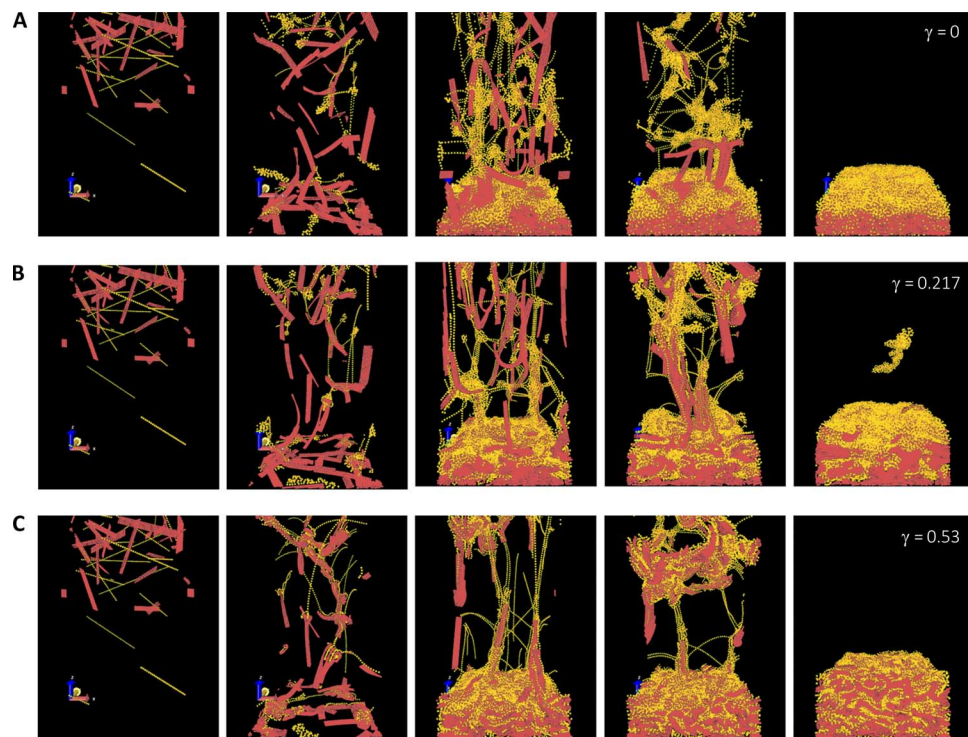
Downloaded from https://www.science.org on May 14, 2025

Fig. 1. Coarse-grained computational MD simulations of SNF/HAP assembly and deposition. Elastic network models are built on mechanics and geometry feature of the unit building blocks. HAP-SNF surface energy γ (J/m^2) is not certain because it depends on the molecular structure and the hierarchy structure of the interface in contact. This is important in forming the layered structure. For the SNF/HAP model, HAP and SNF particles were randomly distributed initially and then subjected to a gravity field that accounts for the drag force from the water flow. (**A** to **C**) Snapshots of the HAP/SNF assembly process during deposition, with γ set as 0 (A), 0.217 J/m^2 (B), and 0.53 J/m^2 (C).

SNFs were used as starting materials. In contrast to our previous liquid exfoliation (top-down) routes for the SNF formation, here, we develop a new and more energetically efficient approach to produce SNFs, controlling the self-assembly of the silk protein (see Fig. 2A and section S3 for more details). First, aqueous silk solution [0.1 weight % (wt %)] was assembled into elongated SNFs with a height of ~3 nm and a contour length of up to 5 μm after heating. Second, the SNFs were used as templates to grow HAP nanocrystals with needle-like structure through in situ biomineralization. These HAP nanocrystals, with a length of 100 to 300 nm and a width of 20 to 30 nm, showed a uniform needle-like morphology and was stabilized by the connected SNF networks; thus, these HAP nanocrystals were finely dispersed and highly stable in the SNF solution (Fig. 2A), in contrast to the flower-like HAP aggregates in silk solution from control experiments (see section S4). Finally, the SNF/HAP dispersion was assembled into water-insoluble macroscopic membranes via vacuum filtration (Fig. 2B). The thickness of the membranes is adjusted by controlling the volume of the SNF/HAP dispersion during processing because they have a linear relationship (fig. S10). The 4-μm-thick membranes (Fig. 2B) can be easily removed from the supporting substrate and exhibit excellent mechanical flexibility (section S5). For example, 37-μm-thick membranes have a

modulus of 7.7 ± 0.2 GPa, around three times higher than the moduli of pristine self-assembled SNF membrane (2.25 ± 0.25 GPa) and liquid-exfoliated SNF membrane (3.5 ± 0.3 GPa) (11, 37). With regard to toughness, the SNF/HAP membranes have a value of 1.7 ± 0.3 MJ/m^3, 10 to 100 times higher than that of SNF membranes (0.09 to 0.2 MJ/m^3) (11, 37). This property ensures the durability of SNF/HAP membranes during the standby and high-pressure purification processes.

These SNF/HAP membranes show highly ordered multilayer structures with ~200-nm-thick alternated HAP and SNF layers (a 4-μm-thick membrane as an example; Fig. 2B). The number of layers is tunable by changing the consumption of dispersion (Fig. 3). Typically, 1 ml of ~0.2 wt % dispersion generates a double-layer membrane, with HAP settling in the bottom layer and the SNF remaining on the top (Fig. 3, A and B). Each layer has a similar thickness of approximately 500 nm. Both layers have uniform dispersions of SNFs and HAPs, respectively, but they show distinct pore sizes (Fig. 3, C and D). The SNF layer has a narrow pore size distribution with a diameter of 8 ± 2 nm (can serve as a size selectivity layer). In contrast, the HAP layer has a larger pore size distribution with a diameter of 28 ± 5 nm (can enhance the water permeation). By progressively adding the volume of the SNF/HAP dispersion, the number of layers is increased and reaches tens of layers
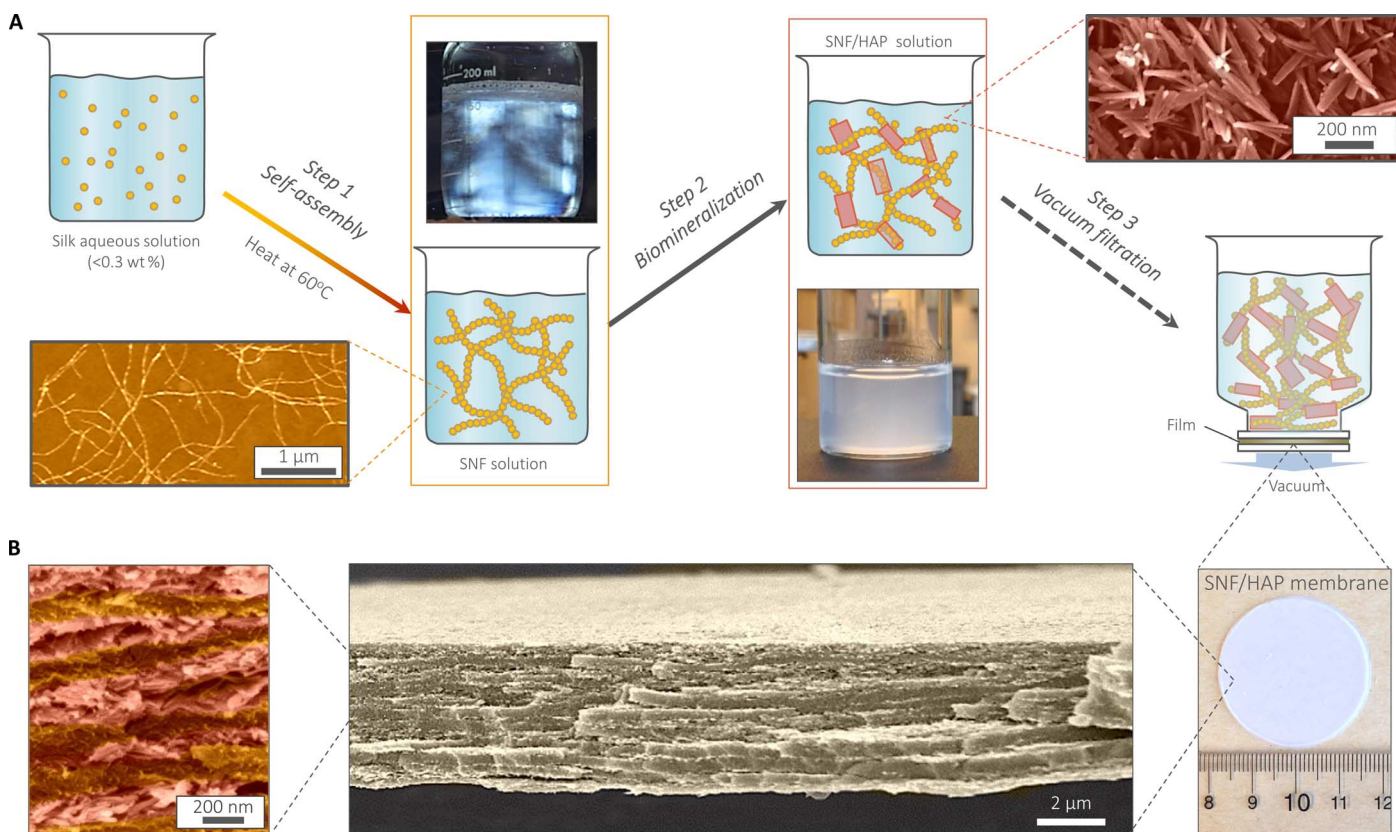
Fig. 2. The pathway to fabricate the SNF/HAP membranes and visualization of typical multilayer structures formed. (**A**) Schematic of the preparation steps of SNF/HAP membranes. Step 1: Silk was assembled to SNFs in aqueous solution. The bottom image in the first row is an atomic force microscopy (AFM) image of SNFs; the top image in the second row is the SNF solution under polarized light, indicating the presence of a nematic phase of SNFs. Step 2: The SNFs were used as templates to induce the growth of HAP nanocrystals. The bottom image in the third row is an image of SNF/HAP solution; the top image in the fourth row is a scanning electron microscopy (SEM) image of biomineralized HAP nanocrystals. Step 3: SNF/HAP dispersions were assembled into membranes via vacuum filtration. (**B**) Multilayer structures of the membranes. The third image is an SNF/HAP membrane with a thickness of 4 μm. This membrane was directly moved from the supporting substrate after filtration of the SNF/HAP dispersion in a process that took 9 s. The second image is the cross-sectional SEM image of SNF/HAP membrane, which shows nacre-like, highly ordered multilayer structures. The first image is the high-resolution cross-sectional SEM of an SNF/HAP membrane. The clear SNF- and HAP-rich layers can be observed. False color was used in AFM and SEM images.
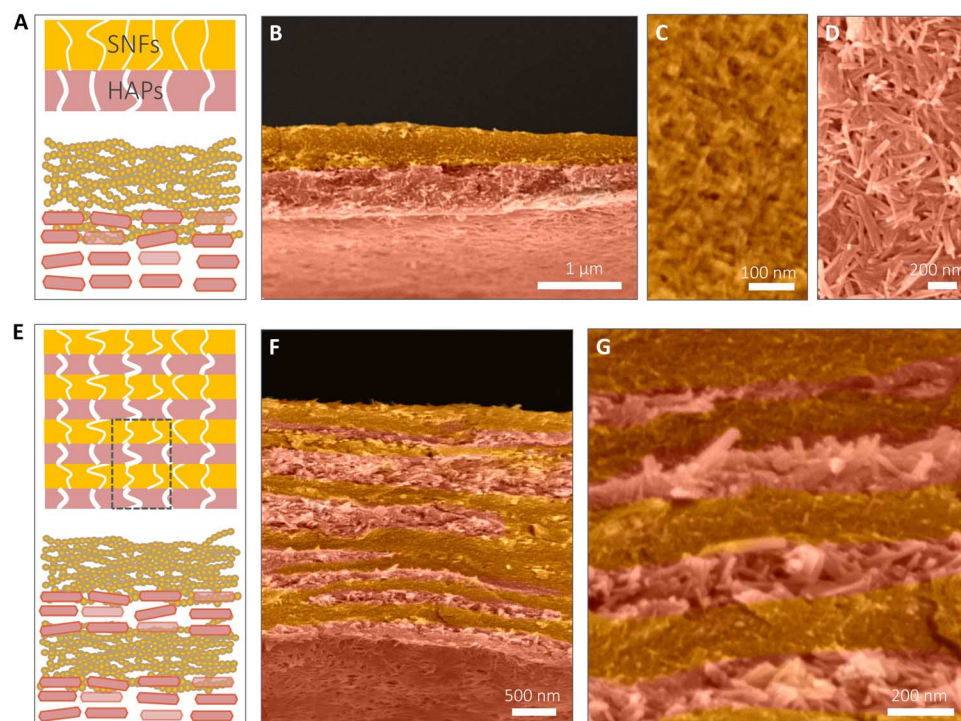
Fig. 3. The well-organized multilayer structures of SNF/HAP membranes. (A to **D)** The double-layer structure of the SNF/HAP membranes was formed through vacuum filtration of 1 ml of dispersion. (A) Schematic of double-layer structures. The top layer is the SNF-rich layer with small pore sizes. The bottom layer is the HAP layer with larger pore sizes. (B) Cross-sectional SEM image of a double-layer membrane. (C and D) Top-view SEM images of SNF-rich (C) and HAP-rich (D) layers. (**E** to **G**) The multilayer structure of the SNF/HAP membrane was generated from 3-ml SNF/HAP dispersion using a 3.5-cm-diameter mold. (E) Schematic of multilayer structures. (F) Cross-sectional SEM image of a multilayer membrane. (G) High-resolution cross-sectional SEM image of a multilayer membrane. False color is used in SEM images.

(Fig. 3, F and G, and section S6). The alternating arrangement of SNF and HAP layers can be observed in all cases.

Another unique advantage of SNF/HAP membranes is their rapid and diversified formation process (Fig. 4, A to C). For example, the 4-μm-thick membrane only required 9 s under vacuum fabrication at 80 kPa (Fig. 4D). These membranes can also be formed directly on a commercial syringe filter by hand-operated extrusion (Fig. 4B). Profiting from the SNF/HAP networks in solution, SNF/HAP composites can stand on support substrates with pore sizes that are much larger (more than 100 times) than their own sizes, such as a 5-μm syringe macrofilter and 40- to 50-μm glass filters (section S7). As controls, other materials, such as top-down SNF and graphene oxide, however, directly pass through the filter (section S7). As a result, in addition to making pressure-driven filtration membranes (Fig. 4C), this SNF/HAP dispersion is suitable for producing highly permeable syringe ultrafilters (Fig. 4B and movie S4), even when a commercial syringe filter with a maximum pore size (the lowest cost systems) is used.

Next, the water flux of SNF/HAP membranes is assessed. Remarkably, fluxes of 0.3-μm-thick SNF/HAP membranes are up to 8355 liter hour^{-1} m^{-2} bar^{-1}, more than 1000 times higher than those of commercial filtration membranes (41–43) and more than 4 times higher than those of most advanced, recently reported ultrathin membranes with similar thicknesses (Fig. 4E) (4, 5, 9–11, 18, 20, 21). In addition, the flux of the SNF/HAP membranes is stable in a 24-hour filtration assessment (Fig. 4F) and much higher than that of both pure SNF membranes with similar thicknesses and the Hagen-Poiseuille theory of uniform materials (9, 44), more consistent with mechanical models for multilayer structures (Fig. 4E and section S8). These results

indicate that the multilayer structures in the membrane do enhance the flux of water through the membranes with similar diameters and thicknesses.

The separation performance of membranes for proteins, colloids, and dyes confirms their universality for water purification (Fig. 4G). In these processes, we used a continuous feeding model with a constant pressure of 80 kPa and calculated rejection at 10 min, 2 hours, and 24 hours of flow (Fig. 4G). Because of the size selectivity and adsorption of membranes, the rejection of all model compounds (Fig. 4G) at 10 min is higher than 64.9%, superior to that found in other polymer-based membranes and similar to other types of protein-based ultrafiltration membranes, such as ferritin and SNF membranes (9, 11). Although the membrane rejection for several compounds (that is, bovine serum albumin, Eosin B, and Orange G) drops significantly at an extremely large volume filtration (more than 1 liter, 24 hours of flow), the membranes exhibit higher water purification ability than do other water purification membranes (10, 11, 14) at hundred milliliter scale. Similar to other ultrafiltration membranes, the flow rates of dye solutions decline gradually with the increase of filtration time (Fig. 4F), because the dye molecules block the membrane pores. However, benefiting from the large pore size and high porosity in the HAP layers, the flux of dye solutions is still larger than 462.9 liter hour^{-1} m^{-2} bar^{-1} after 24 hours of flow. A more detailed discussion about dye separation and adsorption performance of SNF/HAP membranes can be found in section S9. Figure 4H compares the separation efficiencies of SNF/HAP membranes for 5-nm gold nanoparticles with other water purification membranes reported in the literature (4–6, 10, 11, 14, 15, 17, 21). The SNF/HAP membranes extend the "instep" pattern of the reported thickness
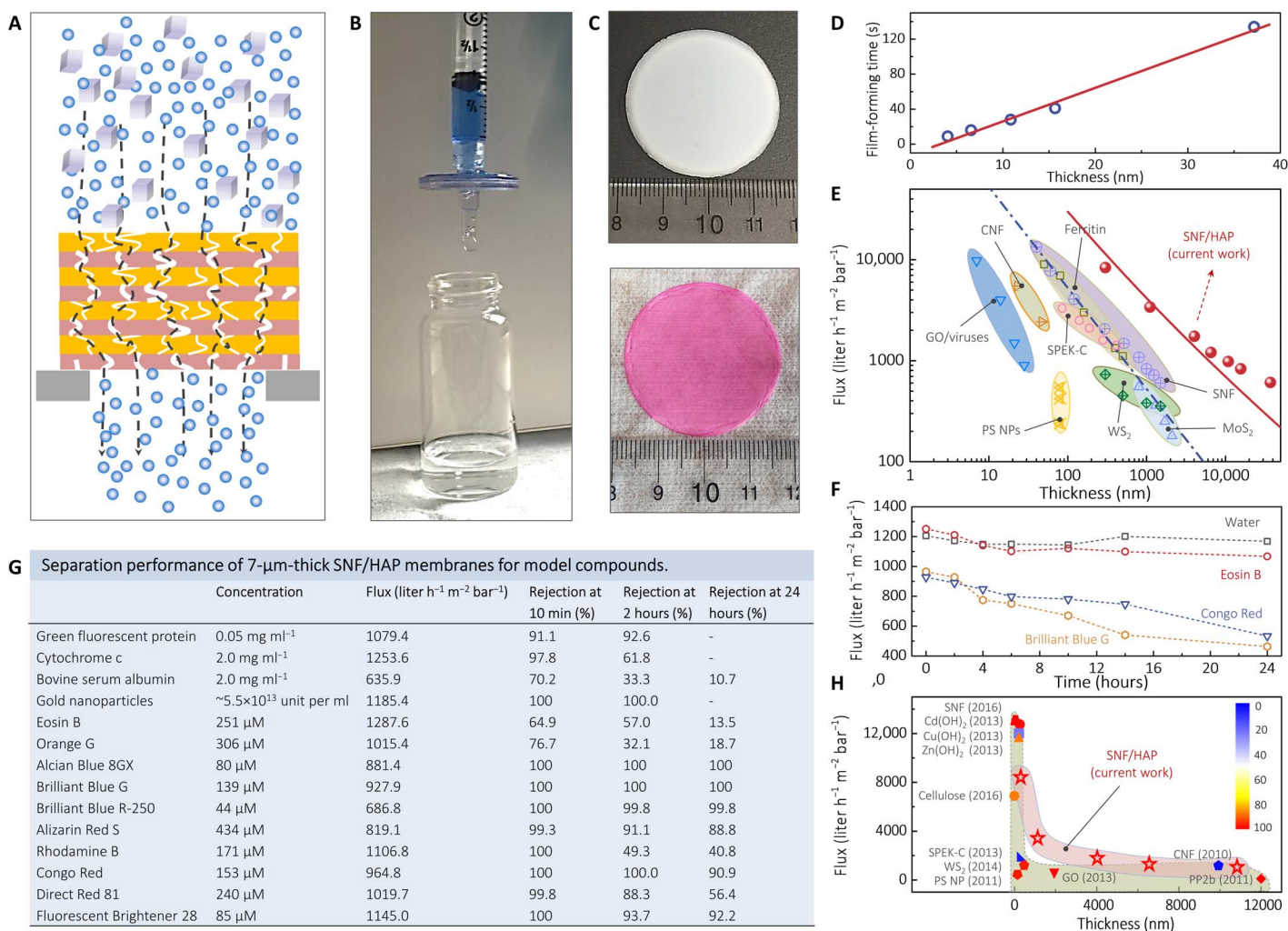
Fig. 4. Separation performance of SNF/HAP membranes. (**A**) Cross-sectional representation of a multilayer SNF/HAP membrane to filter compounds. (**B**) Image of the SNF/HAP-based syringe nanofilter, which successfully rejected Alcian Blue 8GX with a rejection of 98%. The detailed structures of SNF/HAP membranes formed on microfilters can be found in fig. S16B. (**C**) SNF/HAP nanofiltration membrane before (top) and after (bottom) filtration with 20 ml of 5 mM Rhodamine B solution. (**D**) Linear relationship between film thickness and film formation processing time. (**E**) Thickness-dependent changes in permeability to pure water for the SNF/HAP membranes and other previously reported membranes. The blue dash-dot line is a fitted curve using the Hagen-Poiseuille equation with uniform structure (9, 44). The red solid line is a fitted curve using Eq. 1 for multilayer membrane (see also section S8). (**F**) Time-dependent changes in the flux of water and dye solution within 24 hours of flow. (**G**) Separation performance of 7-μm-thick SNF/HAP membranes for dyes, proteins, and colloids after 10 min, 2 hours, and 24 hours of flow. The flux listed in the table was calculated from the filtration of model compound solutions. The filtration pressure was kept at 80 kPa in all these tests. Several dye solutions have lower flux than pure water, likely because of their large molecular size, which would be responsible for blocking the pores of membranes. (**H**) Comparison of the 5-nm gold nanoparticle separation performance of SNF/HAP membranes to that of other filtration membrane materials. The rejection is represented by the color of the pattern. The blue and red are 0 and 100% rejection, respectively. Cd(OH)$_2$, Cu(OH)$_2$, and Zn(OH)$_2$ are Cd(OH)$_2$, Cu(OH)$_2$, and Zn(OH)$_2$ nanofibers. Cellulose, cellulose nanofibers; SPEK-C, sulfonated polyetherketone with cardo groups; WS$_2$, chemically exfoliated tungsten disulfide nanosheets; PS NP, polystyrene nanoparticles; GO, graphene oxide sheets; CNF, carbonaceous nanofiber; PP2b, 5,5′-bis(1-ethynyl-7 polyethylene glycol-*N*,*N*′-bis(ethylpropyl) perylene-3,4,9,10-tetracarboxylic diimide)-2,2′-bipyridine.

versus flux relationship and exhibit a more effective integration of thickness, flux, and separation performance.

Moreover, both SNF and HAP components have exhibited excellent adsorption of heavy metal ions (45); thus, SNF/HAP membranes can be used to remove heavy metal ions (Fig. 5, A and B). Removing metal ions is a formidable but critical task for water purification because heavy metal ions, such as Ni^{2+}, Cr^{3+}, and Pb^{2+}, tend to accumulate in living organisms and are toxic and carcinogenic (Fig. 5D) (46). Therefore, the concentration of metal ions is strictly restricted to trace levels in drinking water. According to the World Health Organization guidelines for drinking water quality (47), the concentrations of Cu^{2+}, Ni^{2+}, Cr^{3+}, and Pb^{2+} should be lower than 2, 0.07, 0.05, and 0.07 mg/liter, respectively (Fig. 5D). Although membrane-based technologies have advantages for heavy metal removal, such as ease of operation and space savings (48), their removal efficiencies are often poor because the pore sizes of the membranes are larger than those of the dissolved metal ions. The mechanism by which SNF/HAP membranes remove metal ions is derived from evidence that both the SNF and HAP components can interact with metal ions through chelation and ion exchange, respectively (49, 50).

Adsorption capacities of SNF/HAP multilayer membranes for metal ions are evaluated via a flux-controllable filtration process (see
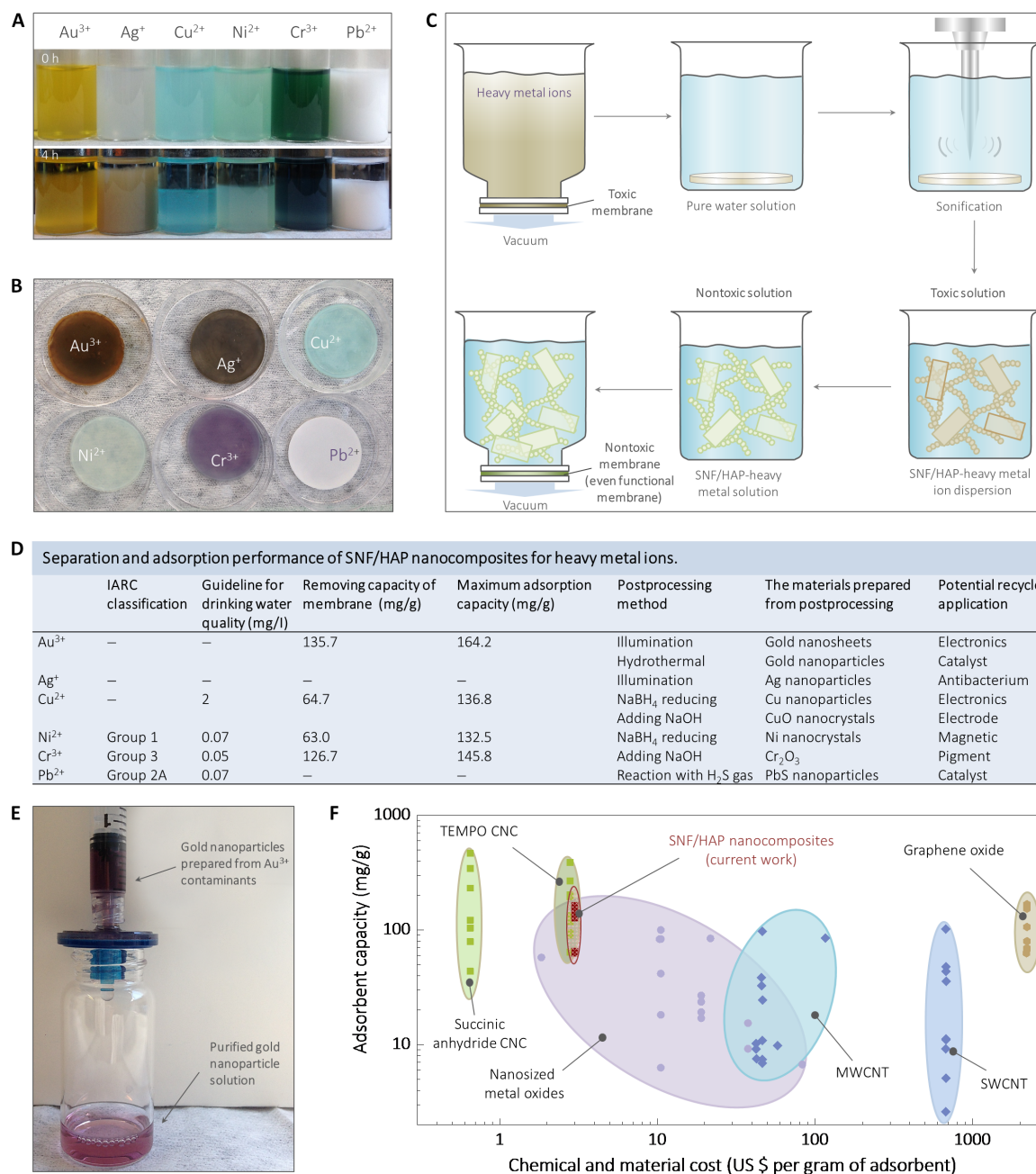
Fig. 5. Removal and recycling of heavy metal ions by SNF/HAP membranes. (**A**) Image of SNF/HAP dispersion-adsorbed metal ions at 0 and 24 hours (see section S10 for more details). (**B**) Image of an SNF/HAP membrane after metal ions were adsorbed through flux-controllable filtration. (**C**) Schematic of a general route for recycling metal ion contaminants by redispersion of saturated SNF/HAP membrane (see section S11 for more details). (**D**) Table of separation and adsorption performance of SNF/HAP nanocomposites for heavy metal ions (see section S10 for more details). The adsorbent capacity of Ag^+ and Pb^{2+} is not listed quantitatively because Ag^+ and Pb^{2+} interacted with Cl^- to yield a precipitate. The maximum adsorption capabilities of SNF/HAP composite for metal ions were calculated from equilibrium adsorption isotherms data (see section S10 for details). IARC, International Agency for Research on Cancer. (**E**) Gold contaminants can be reused after facile and green postprocessing (see section S11 for more details about postprocessing for metal ions). (**F**) Cost and adsorption capacity estimates for the most-studied nanomaterials. The detailed calculations and comparisons of these materials are shown in section S12. TEMPO, 2,2,6,6-tetramethylpiperidine 1-oxyl; MWCNT, multi-walled carbon nanotube; SWCNT, single-walled carbon nanotube.

section S10) with values of at least 63.0 mg/g (Ni^{2+}), which are much higher than those found for other types of ultrafiltration membranes (*9*, *11*). The detailed adsorption kinetic and isotherm experiments and discussion of SNF/HAP nanocomposites for heavy metal ions can be found in section S10. Moreover, the metal ions adsorbed by the SNF/

HAP membranes can be recycled and transferred to nontoxic nanomaterials via a universal, simple, and harmless postprocessing approach (see Fig. 5C and section S11 for more details). Briefly, the saturated membranes were redispersed in water by ultrasonication. Postprocessing was then applied to synthesize nontoxic nanomaterials

or reusable functional nanomaterials, followed by the assembly of these nontoxic nanomaterial dispersions into bulk materials to avoid producing potentially toxic nanomaterials (Fig. 5E). After this recycling process, at least 92 ± 4% (Au^{3+}) of ion contaminants are removed and do not yield any secondary pollutants.

The broad acceptance of novel water purification nanotechnologies depends on their performance and affordability (51). Figure 5F and section S12 summarize the cost estimation versus adsorbent capacity of the most studied nanomaterials. The SNF/HAP composites show optimum performance in terms of both price and adsorbent capacity. The cost of SNF/HAP membrane is approximately $3.36 per gram, which is comparable with that of cellulose nanocrystal (CNC) materials ($0.65 to $2.80). In terms of adsorbent capacity, SNF/HAP membranes are better than other inorganic nanomaterials and similar to the CNC hydrogels; however, because of the additional size-exclusion affinity of SNF/HAP membrane for dyes or other molecular contaminants, the SNF/HAP membranes are much more effective for water treatment than CNC hydrogels.

DISCUSSION

In summary, we report a new and optimized biomimetic route to fabricate biomaterial-based multilayer membranes for water purification, which consists of well-organized multilayer structures through silk self-assembly and in situ HAP biomineralization. These low-cost SNF/HAP membranes exhibit universal water purification capability for dyes, proteins, and nanocolloids. Moreover, the membranes can be formed from SNF/HAP dispersions under a short processing time, enabling the fabrication of multitype purification membranes, such as pressure-derived filtration membranes and syringe ultrafilters. More remarkably, SNF/HAP membranes can be used to remove metal ions, a unique feature in comparison to the capabilities of other nanofiltration membranes. The metal ion contaminants that are removed can also be reused by simple green routes to avoid secondary pollutants. These outcomes demonstrate the strong potential for this study for use of these new systems in a wide range of applications, such as wastewater treatment, nanotechnology, food industry, and the life sciences. Initially, we selected SNFs as starting materials. On the basis of our simulation results, different protein-based fibrils (that is, amyloid and collagen fibril) and their corresponding biomineral systems (that is, calcification and silicification) may be suitable for building multilayer structures in a similar fashion as demonstrated here for the SNF and HAP. In addition, engineered peptides and proteins, such as silk-, silk-elastin–, silaffin-, and apatite-binding peptide–based peptides and proteins, are also useful starting materials because the interaction between these peptides and proteins with minerals can be evaluated and predicted by computational simulation. We can choose the optimized protein/mineral combination according to the in silico predictions to design and fabricate the desired multilayer (or uniform) constructions. This interaction between simulation and experiment not only allows larger design space for the materials but also improves the efficiency in the design of new materials with definable structures and properties.

MATERIALS AND METHODS
Preparation of SNF solution
First, *Bombyx mori* silkworm cocoon silk fibers were degummed by boiling in two 30-min changes of 0.5% (w/w) $NaHCO_3$ solution. Then,

the degummed silk fibers were washed with distilled water and allowed to air-dry at room temperature. Next, a 10% (w/v) solution of degummed silk fibroin (SF) in aqueous 9.3 M LiBr solution was prepared by heating to 60°C for 1 hour. This solution was dialyzed with deionized water at room temperature to yield SF solution with a protein concentration of ~5 wt %. To grow SNFs, this solution was further adjusted to 0.1 wt % SF in aqueous solutions and incubated without any perturbation at 60°C over 7 days. The structural details of SNFs were characterized by AFM (Asylum Research, Oxford Instruments Company).

Synthesis of HAP nanocrystals via biomineralization approach
Our process was inspired by biomineralization behavior in nature: SNFs were used as capping agents and templates for mineral formation and growth. Specifically, 6 ml of 0.2 M $CaCl_2$ was added to 100 ml of SNF solution (0.1 wt %) under continuous stirring or agitation. Five minutes later, 6 ml of 0.2 M Na_2HPO_4 was introduced, and the mixture was incubated at 37°C for 1 week to grow the HAP nanocrystals. The synthetic HAP nanocrystals were confirmed by x-ray diffraction (XRD) measurements [Bruker D8 Discover diffractometer with the two-dimensional detector of General Area Detector Diffraction System (GADDS)]. The experiment was performed at the Massachusetts Institute of Technology Center for Materials Science and Engineering. Their structural features were disclosed by Ultra 55 field-emission SEM (Carl Zeiss AG).

The preparation of SNF/HAP membranes
All the SNF/HAP membranes were fabricated by vacuum filtration of the SNF dispersions through a vacuum filtration assembly and polycarbonate (PC) filtration membranes (pore size, 200 nm; diameter, 47 mm; Sigma-Aldrich).

Coarse-grained simulation of NF/NP assembly
MD simulations were run with the Large-Scale Atomic/Molecular Massively Parallel Simulator (LAMMPS) molecular simulation package (52). Elastic network models were built in mechanics and geometry feature of the unit building blocks. Each NF flake and NP thread were modeled by an elastic network with mass concentrated at the junction beads to match the material densities, following the similar strategy that has been applied to modeling other biological materials (53). In the SNF/HAP system, as an example, an SNF was modeled by a series of mass beads connected by a series of harmonic springs, and a HAP flake was modeled by mass beads connected by a rectangular spring network. The total energy of each SNF/HAP unit is given by

$$E = E_T + E_B + E_{nonbond} \qquad (1)$$

where E_T is the tensile deformation energy for fiber stretching, E_B is for bending, and $E_{nonbond}$ is for nonbonded interaction with other SNF and HAP beads. The mathematical expressions of E_T and E_B contain carefully chosen elastic numerical constants to match the materials' elastic properties (see section S2 for detailed parameters).

The interaction between a pair of nonbonded SNF/HAP beads was determined by the HAP-SNF surface energy γ, which was not certain because it depended on the molecular structure, chemical environment, and hierarchy structure of the interface in contact. Its value was tuned in our simulations, and we discovered that it could be used

as a key parameter to govern the morphology of the layered structure. The simulation box size was 0.5 μm × 0.5 μm × 50 μm, with 50 μm along the axis of the flow direction, and periodic boundary conditions were applied to the other two directions. A collection of SNFs was generated, with their length distribution similar to that of experimental measurements, which has a mean value of 1 μm and an SD of 0.4 μm. The HAP model was built according to experimental measurements of the typical mineral size as 6 nm × 30 nm × 240 nm. The ratios of numbers of SNF and HAP molecules were computed according to their experimental volume ratios in solution. The volume ratios of both HAP and SNF were increased 16 times to account for the effect of getting concentrated at the bottom of the bottle and to overcome the limitation of size and time of simulations. Each SNF and HAP was initially randomly placed and oriented in the simulation box, as shown in fig. S2A. More details can be found in section S2.

Computational modeling of the effect of flow

We implicitly modeled the water flow by applying the drag force to all the coarse-grained beads. HAP and SNF beads were subjected to a gravity field that accounts for the drag force from the water flow. The drag force was given by the Stokes' law as

$$f_{drag} = -6\pi\mu R\nu \tag{2}$$

where R is the effective bead radius for SNF and HAP materials (see section S6 for detailed values), $\mu = 8.6 \times 10^{-4}$ Pa · s is the fluid viscosity constant of water at room temperature, and $\nu = 250$ m/s is the flow velocity we used in our simulations, and its large numerical value is used to overcome the limitation of time scale in simulation. All the numerical values of the physical parameters of the model are summarized in table S1.

The interaction between simulation and experiment for material design

The numerical values of the physical parameters of the SNF and HAP were based on the former studies of atomistic simulations, whereas values for chemical concentrations and particle geometries were obtained from experimental measurements in SEM. After computational simulation, the simulation result of the multilayer material (Fig. 1A) formed in silico was compared to the experimental observation in SEM (Fig. 3), and an agreement was found. Simulations showed that the multilayer membrane could only be formed with a relatively low SNF/HAP interaction. We have experimental evidence to show that SNF can easily exfoliate from the HAP surface to validate this conclusion.

Theoretical water flux of the SNF/HAP membrane

Starting from the Hagen-Poiseuille equation (44), the water flux of the SNF/HAP multilayer membrane was derived and given by

$$f_{flux} = \frac{\pi(h_1 + h_2)}{8\mu H\left(\frac{h_1}{\beta_1 r_2^4} + \frac{h_2}{\beta_2 r_2^4}\right)} \tag{3}$$

where H is the total thickness, μ is the viscosity of water, and h_i and r_i are the average thickness and the average radius of the pores, respectively, with lower index 1 for the SNF layer and lower index 2 for the HAP layer. β_i accounts for the pore's surface density and shape factor (see section S8 for detailed derivations).

Separation performance measurements

The separation was performed on a vacuum filtration device (glass vacuum filtration assembly device, Sigma-Aldrich; membrane diameter, 47 mm; inner diameter of funnel top, 35 mm). For flux assessments, we followed the method used for other ultrathin membranes (4–6, 10, 11, 14, 15, 17, 21). Typically, water or model compound solutions were filtered through the as-prepared membranes, which stand on a porous support membrane. The flux (J; in liter hour^{-1} m^{-2} bar^{-1}) is calculated by $J = V/(Atp)$, where V is the volume of the water filtered (in liters), A is the effective membrane filtration area (in square meters), t is the filtration time (in hours), and p is the suction pressure across the membrane (in bars). Here, note that A is the effective membrane filtration area instead of the membrane area. The effective filtration area is determined by membrane area and porosity of support membrane. In the present experiments, the filtration area of the filter holder is 9.62 cm^2 and the porosity of the support membrane (PC membrane; pore size, 200 nm) is 10%. Thus, the effective surface area is 0.962 cm^2. The separation preformation evaluations were carried out by continuous 24-hour uninterrupted filtration, with a constant pressure of 80 kPa. Permeation was characterized by ultraviolet-visible (UV-vis) spectroscopy and fluorescence spectrophotometry (SpectraMax M2, Molecular Devices) and inductively coupled plasma atomic emission spectrometry (ICP-AES; Prodigy High Dispersion ICP, Teledyne Leeman Labs). Rejection (R; %) was calculated by

$$R = \left(1 - \frac{C_p}{C_f}\right) \times 100\% \tag{4}$$

where C_f and C_p are the concentrations of the compounds in the feed and permeate, respectively. Additional information on materials, characterization, and simulations can be found in the Supplementary Materials.

Adsorption experiments

The adsorption experiments were carried out to evaluate the adsorption performance of dyes and heavy metals on the SNF/HAP composites. All dye and metal ion aqueous solutions were prepared using deionized water. The solutions of different concentrations used in various experiments were obtained by diluting stock solutions. For dye adsorption experiments, Rhodamine B, Congo Red, and Brilliant Blue G were chosen to conduct experiments because these dyes have different molecular sizes, charges, and structural features (see Fig. 4G for details). The initial concentration and volume of dye aqueous solutions for different experiments can be found in section S9. In these experiments, the freshly prepared SNF/HAP membranes were directly transferred to well-capped dye aqueous solutions and allowed to stand at room temperature for 48 hours to reach adsorption equilibrium. In terms of metal ion adsorption experiments, the Au^{3+}, Cu^{2+}, Ni^{2+}, and Cr^{3+} ion aqueous solutions were selected to evaluate the adsorption performance of SNF/HAP composites. First, the 0.2 wt % SNF/HAP solution was concentrated by vacuum filtration to remove most of the water in solution. The resultant slurry was then processed by freeze-drying to obtain SNF/HAP adsorbents. All the sorption tests were conducted in capped 600-ml flasks containing 150 ml of metal ion aqueous solutions, which were prepared using deionized water. The initial metal ion concentrations of adsorption isotherms and kinetic experiments were set as 100 and 10 mg liter^{-1}, respectively. The dosage of SNF/HAP adsorbents was increased gradually from 50 to 350 mg.

After adsorption, the adsorbent was filtrated using a 0.2-μm membrane. The residual metal ion concentrations in the solutions were determined by an ICP-AES. More detailed experimental conditions and discussion can be found in section S10. The modeling of adsorption isotherms and kinetic experiments is presented in section S1.

SUPPLEMENTARY MATERIALS

REFERENCES AND NOTES

1. J. R. Werber, C. O. Osuji, M. Elimelech, Materials for next-generation desalination and water purification membranes. Nat. Rev. Mater. 16018 (2016).
2. P. Vandezande, L. E. M. Gevers, I. F. J. Vankelecom, Solvent resistant nanofiltration: Separating on a molecular level. Chem. Soc. Rev. 37, 365–405 (2008).
3. M. A. Shannon, P. W. Bohn, M. Elimelech, J. G. Georgiadis, B. J. Mariñas, A. M. Mayes, Science and technology for water purification in the coming decades. Nature 452, 301–310 (2008).
4. Q. Zhang, S. Ghosh, S. Samitsu, X. Peng, I. Ichinose, Ultrathin freestanding nanoporous membranes prepared from polystyrene nanoparticles. J. Mater. Chem. 21, 1684–1688 (2011).
5. C. Deng, Q. G. Zhang, G. L. Han, Y. Gong, A. M. Zhu, Q. L. Liu, Ultrathin self-assembled anionic polymer membranes for superfast size-selective separation. Nanoscale 5, 11028–11034 (2013).
6. E. Krieg, H. Weissman, E. Shirman, E. Shimoni, B. Rybtchinski, A recyclable supramolecular membrane for size-selective separation of nanoparticles. Nat. Nanotechnol. 6, 141–146 (2011).
7. X. S. Peng, J. Jin, I. Ichinose, Mesoporous separation membranes of polymer-coated copper hydroxide nanostrands. Adv. Funct. Mater. 17, 1849–1855 (2007).
8. Q. Wang, S. Samitsu, I. Ichinose, Ultrafiltration membranes composed of highly cross-linked cationic polymer gel: The network structure and superior separation performance. Adv. Mater. 23, 2004–2008 (2011).
9. X. Peng, J. Jin, Y. Nakamura, T. Ohno, I. Ichinose, Ultrafast permeation of water through protein-based membranes. Nat. Nanotechnol. 4, 353–357 (2009).
10. Q. G. Zhang, C. Deng, F. Soyekwo, Q. L. Liu, A. M. Zhu, Sub-10 nm wide cellulose nanofibers for ultrathin nanoporous membranes with high organic permeation. Adv. Funct. Mater. 26, 792–800 (2016).
11. S. Ling, K. Jin, D. L. Kaplan, M. J. Buehler, Ultrathin free-standing Bombyx mori silk nanofibril membranes. Nano Lett. 16, 3795–3800 (2016).
12. S. Bolisetty, R. Mezzenga, Amyloid–carbon hybrid membranes for universal water purification. Nat. Nanotechnol. 11, 365–371 (2016).
13. J. He, X.-M. Lin, H. Chan, L. Vuković, P. Král, H. M. Jaeger, Diffusion and filtration properties of self-assembled gold nanocrystal membranes. Nano Lett. 11, 2430–2435 (2011).
14. S. Karan, Q. Wang, S. Samitsu, Y. Fujii, I. Ichinose, Ultrathin free-standing membranes from metal hydroxide nanostrands. J. Membr. Sci. 448, 270–291 (2013).
15. H.-W. Liang, L. Wang, P.-Y. Chen, H.-T. Lin, L.-F. Chen, D. He, S.-H. Yu, Carbonaceous nanofiber membranes for selective filtration and separation of nanoparticles. Adv. Mater. 22, 4691–4695 (2010).
16. S. J. Gao, H. Qin, P. P. Liu, J. Jin, SWCNT-intercalated GO ultrathin films for ultrafast separation of molecules. J. Mater. Chem. A 3, 6649–6654 (2015).
17. H. Huang, Z. Song, N. Wei, L. Shi, Y. Mao, Y. Ying, L. Sun, Z. Xu, X. Peng, Ultrafast viscous water flow through nanostrand-channelled graphene oxide membranes. Nat. Commun. 4, 2979 (2013).
18. Y. M. Lee, Y. Jung, Y. H. Kim, A. R. Park, S. Han, W.-S. Choe, P. J. Yoo, Nanomesh-structured ultrathin membranes harnessing the unidirectional alignment of viruses on a graphene-oxide film. Adv. Mater. 26, 3899–3904 (2014).
19. R. K. Joshi, P. Carbone, F. C. Wang, V. G. Kravets, Y. Su, I. V. Grigorieva, H. A. Wu, A. K. Geim, R. R. Nair, Precise and ultrafast molecular sieving through graphene oxide membranes. Science 343, 752–754 (2014).

20. L. Sun, H. Huang, X. Peng, Laminar MoS$_2$ membranes for molecule separation. *Chem. Commun.* **49**, 10718–10720 (2013).

21. L. Sun, Y. Ying, H. Huang, Z. Song, Y. Mao, Z. Xu, X. Peng, Ultrafast molecule separation through layered WS$_2$ nanosheet membranes. *ACS Nano* **8**, 6304–6311 (2014).

22. H. Choi, A. C. Sofranko, D. D. Dionysiou, Nanocrystalline TiO$_2$ photocatalytic membranes with a hierarchical mesoporous multilayer structure: Synthesis, characterization, and multifunction. *Adv. Funct. Mater.* **16**, 1067–1074 (2006).

23. C. C. Striemer, T. R. Gaborski, J. L. McGrath, P. M. Fauchet, Charge- and size-based separation of macromolecules using ultrathin silicon membranes. *Nature* **445**, 749–753 (2007).

24. A. Eguizábal, M. Sgroi, D. Pullini, E. Ferain, M. P. Pina, Nanoporous PBI membranes by track etching for high temperature PEMs. *J. Membr. Sci.* **454**, 243–252 (2014).

25. S. Karan, S. Samitsu, X. Peng, K. Kurashima, I. Ichinose, Ultrafast viscous permeation of organic solvents through diamond-like carbon nanosheets. *Science* **335**, 444–447 (2012).

26. R. Mourhatch, T. T. Tsotsis, M. Sahimi, Network model for the evolution of the pore structure of silicon-carbide membranes during their fabrication. *J. Membr. Sci.* **356**, 138–146 (2010).

27. N. Joseph, P. Ahmadiannamini, R. Hoogenboom, I. F. J. Vankelecom, Layer-by-layer preparation of polyelectrolyte multilayer membranes for separation. *Polym. Chem.* **5**, 1817–1831 (2014).

28. A. M. Balachandra, J. Dai, M. L. Bruening, Enhancing the anion-transport selectivity of multilayer polyelectrolyte membranes by templating with Cu^{2+}. *Macromolecules* **35**, 3171–3178 (2002).

29. X. Liu, M. L. Bruening, Size-selective transport of uncharged solutes through multilayer polyelectrolyte membranes. *Chem. Mater.* **16**, 351–357 (2004).

30. T. R. Farhat, J. B. Schlenoff, Doping-controlled ion diffusion in polyelectrolyte multilayers: Mass transport in reluctant exchangers. *J. Am. Chem. Soc.* **125**, 4627–4636 (2003).

31. V. Smuleac, D. A. Butterfield, D. Bhattacharyya, Layer-by-layer-assembled microfiltration membranes for biomolecule immobilization and enzymatic catalysis. *Langmuir* **22**, 10118–10124 (2006).

32. C. Cheng, A. Yaroshchuk, M. L. Bruening, Fundamentals of selective ion transport through multilayer polyelectrolyte membranes. *Langmuir* **29**, 1885–1892 (2013).

33. K. A. Brauman, G. C. Daily, T. Ka'eo Duarte, H. A. Mooney, The nature and value of ecosystem services: An overview highlighting hydrologic services. *Annu. Rev. Environ. Resour.* 32, 67–98 (2007).

34. J. Borges, J. F. Mano, Molecular interactions driving the layer-by-layer assembly of multilayers. *Chem. Rev.* **114**, 8883–8942 (2014).

35. J. J. Richardson, M. Björnmalm, F. Caruso, Technology-driven layer-by-layer assembly of nanofilms. *Science* **348**, aaa2491 (2015).

36. Y. Li, X. Wang, J. Sun, Layer-by-layer assembly for rapid fabrication of thick polymeric films. *Chem. Soc. Rev.* **41**, 5998–6009 (2012).

37. S. Ling, C. Li, J. Adamcik, Z. Shao, X. Chen, R. Mezzenga, Modulating materials by orthogonally oriented β-strands: Composites of amyloid and silk fibroin fibrils. *Adv. Mater.* **26**, 4569–4574 (2014).

38. P.-Y. Chen, J. McKittrick, M. A. Meyers, Biological materials: Functional adaptations and bioinspired designs. *Prog. Mater. Sci.* **57**, 1492–1704 (2012).

39. C. Meier, M. E. Welland, Wet-spinning of amyloid protein nanofibers into multifunctional high-performance biofibers. *Biomacromolecules* **12**, 3453–3459 (2011).

40. C. Li, A.-K. Born, T. Schweizer, M. Zenobi-Wong, M. Cerruti, R. Mezzenga, Amyloid-hydroxyapatite bone biomimetic composites. *Adv. Mater.* **26**, 3207–3212 (2014).

41. I. F. J. Vankelecom, K. De Smet, L. E. M. Gevers, P. A. Jacobs, Nanofiltration membrane materials and preparation, in *Nanofiltration: Principles and Applications*, A. I. Schöfer, A. G. Fane, T. D. Waite, Eds. (Elsevier, 2005).

42. Y. Lu, T. Suzuki, W. Zhang, J. S. Moore, B. J. Marinas, Nanofiltration membranes based on rigid star amphiphiles. *Chem. Mater.* **19**, 3194–3204 (2007).

43. L. Braeken, B. Van der Bruggen, C. Vandecasteele, Flux decline in nanofiltration due to adsorption of dissolved organic compounds: Model prediction of time dependency. *J. Phys. Chem. B* **110**, 2957–2962 (2006).

44. R. W. Baker, *Membrane Technology and Applications* (John Wiley & Sons, ed. 3, 2012).

45. P. Koley, M. Sakurai, T. Takei, M. Aono, Facile fabrication of silk protein sericin-mediated hierarchical hydroxyapatite-based bio-hybrid architectures: Excellent adsorption of toxic heavy metals and hazardous dye from wastewater. *RSC Adv.* **6**, 86607–86616 (2016).

46. International Agency for Research on Cancer, *Agents Classified by the IARC Monographs (Volumes 49 and 87)* (International Agency for Research on Cancer, 2012); http://monographs.iarc.fr/ENG/Classification/.

47. World Health Organization, *Guidelines for Drinking-Water Quality* (WHO Press, ed. 4, 2011); www.who.int/water_sanitation_health/publications/dwq-guidelines-4/en/.

48. F. Fu, Q. Wang, Removal of heavy metal ions from wastewaters: A review. *J. Environ. Manage.* **92**, 407–418 (2011).

49. R. Rajkhowa, R. Naik, L. Wang, S. V. Smith, X. Wang, An investigation into transition metal ion binding properties of silk fibers and particles using radioisotopes. *J. Appl. Polym. Sci.* **119**, 3630–3639 (2011).

50. J. Reichert, J. G. P. Binner, An evaluation of hydroxyapatite-based filters for removal of heavy metal ions from aqueous solutions. *J. Mater. Sci.* **31**, 1231–1241 (1996).

51. X. Qu, J. Brame, Q. Li, P. J. J. Alvarez, Nanotechnology for a safe and sustainable water supply: Enabling integrated water treatment and reuse. *Acc. Chem. Res.* **46**, 834–843 (2013).

52. S. Plimpton, Fast parallel algorithms for short-range molecular dynamics. *J. Comput. Phys.* **117**, 1–19 (1995).

53. Z. Qin, M. J. Buehler, Impact tolerance in mussel thread networks by heterogeneous material distribution. *Nat. Commun.* **4**, 2187 (2013).

54. Z. Chen, W. Ma, M. Han, Biosorption of nickel and copper onto treated alga (*Undaria pinnatifida*): Application of isotherm and kinetic models. *J. Hazard. Mater.* **155**, 327–333 (2008).

55. Z. Aksu, Determination of the equilibrium, kinetic and thermodynamic parameters of the batch biosorption of nickel(II) ions onto *Chlorella vulgaris*. *Process Biochem.* **38**, 89–99 (2002).

56. J.-S. Wang, R.-T. Peng, J.-H. Yang, Y.-C. Liu, X.-J. Hu, Preparation of ethylenediamine-modified magnetic chitosan complex for adsorption of uranyl ions. *Carbohydr. Polym.* **84**, 1169–1175 (2011).

57. J. Bertaud, Z. Qin, M. J. Buehler, Amino acid sequence dependence of nanoscale deformation mechanisms in alpha-helical protein filaments. *J. Strain Anal. Eng. Des.* **44**, 517–531 (2009).

58. T.-J. Lin, H. Heinz, Accurate force field parameters and pH resolved surface models for hydroxyapatite to understand structure, mechanics, hydration, and biological interfaces. *J. Phys. Chem. C* **120**, 4975–4992 (2016).

59. J.-M. Jung, R. Mezzenga, Liquid crystalline phase behavior of protein fibers in water: Experiments versus theory. *Langmuir* **26**, 504–514 (2010).

60. S. Ling, Z. Qi, D. P. Knight, Z. Shao, X. Chen, Synchrotron FTIR microspectroscopy of single natural silk fibers. *Biomacromolecules* **12**, 3344–3349 (2011).

61. J. Tao, H. Pan, Y. Zeng, X. Xu, R. Tang, Roles of amorphous calcium phosphate and biological additives in the assembly of hydroxyapatite nanoparticles. *J. Phys. Chem. B* **111**, 13410–13418 (2007).

62. H. G. Zhang, Q. Zhu, Glutamic acid-mediated synthesis of ultralong hydroxyapatite nanoribbons under hydrothermal conditions. *Chem. Lett.* **34**, 788–789 (2005).

63. T. Matsumoto, M. Okazaki, M. Inoue, Y. Hamada, M. Taira, J. Takahashi, Crystallinity and solubility characteristics of hydroxyapatite adsorbed amino acid. *Biomaterials* **23**, 2241–2247 (2002).

64. S. Ling, C. Li, K. Jin, D. L. Kaplan, M. J. Buehler, Liquid exfoliated natural silk nanofibrils: Applications in optical and electrical devices. *Adv. Mater.* **28**, 7783–7790 (2016).

65. G. Fang, Y. Yang, J. Yao, Z. Shao, X. Chen, Formation of different gold nanostructures by silk nanofibrils. *Mater. Sci. Eng. C* **64**, 376–382 (2016).

66. Y. Zhou, W. Chen, H. Itoh, K. Naka, Q. Ni, H. Yamane, Y. Chujo, Preparation of a novel core–shell nanostructured gold colloid–silk fibroin bioconjugate by the protein redox technique at room temperature. *Chem. Commun.* **23**, 2518–2519 (2001).

67. M. C. Daniel, D. Astruc, Gold nanoparticles: Assembly, supramolecular chemistry, quantum-size-related properties, and applications toward biology, catalysis, and nanotechnology. *Chem. Rev.* **104**, 293–346 (2004).

68. X. Fei, M. Jia, X. Du, Y. Yang, R. Zhang, Z. Shao, X. Zhao, X. Chen, Green synthesis of silk fibroin-silver nanoparticle composites with effective antibacterial and biofilm-disrupting properties. *Biomacromolecules* **14**, 4483–4488 (2013).

69. I. A. Banerjee, L. Yu, H. Matsui, Cu nanocrystal growth on peptide nanotubes by biomineralization: Size control of Cu nanocrystals by tuning peptide conformation. *Proc. Natl. Acad. Sci. U.S.A.* **100**, 14678–14682 (2003).

70. X. Fei, Z. Shao, X. Chen, Synthesis of hierarchical three-dimensional copper oxide nanostructures through a biomineralization-inspired approach. *Nanoscale* **5**, 7991–7997 (2013).

71. G. N. Glavee, K. J. Klabunde, C. M. Sorensen, G. C. Hadjipanayis, Borohydride reduction of nickel and copper ions in aqueous and nonaqueous media. Controllable chemistry leading to nanoscale metal and metal boride particles. *Langmuir* **10**, 4726–4730 (1994).

72. M. Kowshik, W. Vogel, J. Urban, S. K. Kulkarni, K. M. Paknikar, Microbial synthesis of semiconductor PbS nanocrystallites. *Adv. Mater.* **14**, 815–818 (2002).

73. K. Numata, P. Cebe, D. L. Kaplan, Mechanism of enzymatic degradation of beta-sheet crystals. *Biomaterials* **31**, 2926–2933 (2010).

74. Y.-H. Chen, F.-A. Li, Kinetic study on removal of copper(II) using goethite and hematite nano-photocatalysts. *J. Colloid Interface Sci.* **347**, 277–281 (2010).

75. J. Hu, G. H. Chen, I. M. C. Lo, Removal and recovery of Cr(VI) from wastewater by maghemite nanoparticles. *Water Res.* **39**, 4528–4536 (2005).

76. J. Hu, G. Chen, I. M. C. Lo, Selective removal of heavy metals from industrial wastewater using maghemite nanoparticle: Performance and mechanisms. *J. Environ. Eng.* **132**, 709–715 (2006).

77. R. Koivulaa, J. Pakarinenb, M. Sieviusb, K. Sirolab, R. Harjulaa, E. Paaterob, Use of hydrometallurgical wastewater as a precursor for the synthesis of

cryptomelane-type manganese dioxide ion exchange material. *Sep. Purif. Technol.* **70**, 53–57 (2009).

78. J. Pakarinen, R. Koivula, M. Laatikainen, K. Laatikainen, E. Paatero, R. Harjula, Nanoporous manganese oxides as environmental protective materials—Effect of Ca and Mg on metals sorption. *J. Hazard. Mater.* **180**, 234–240 (2010).

79. J. Pakarinen, M. Laatikainen, K. Sirola, E. Paatero, R. Koivula, R. Harjula, Behavior of silica-supported manganese oxides in hydrometallurgical separations. *Sep. Sci. Technol.* **44**, 3045–3074 (2009).

80. X. L. Pu, Z. C. Jiang, B. Hu, H. B. Wang, γ-MPTMS modified nanometer-sized alumina micro-column separation and preconcentration of trace amounts of Hg, Cu, Au and Pd in biological, environmental and geological samples and their determination by inductively coupled plasma mass spectrometry. *J. Anal. At. Spectrom.* **19**, 984–989 (2004).

81. A. Afkhami, M. Saber-Tehrani, H. Bagheri, Simultaneous removal of heavy-metal ions in wastewater samples using nano-alumina modified with 2,4-dinitrophenylhydrazine. *J. Hazard. Mater.* **181**, 836–844 (2010).

82. X. Wang, W. Cai, Y. Lin, G. Wang, C. Liang, Mass production of micro/nanostructured porous ZnO plates and their strong structurally enhanced and selective adsorption performance for environmental remediation. *J. Mater. Chem.* **20**, 8582–8590 (2010).

83. C.-Y. Cao, Z.-M. Cui, C.-Q. Chen, W.-G. Song, W. Cai, Ceria hollow nanospheres produced by a template-free microwave-assisted hydrothermal method for heavy metal ion removal and catalysis. *J. Phys. Chem. C* **114**, 9865–9870 (2010).

84. S. Hokkanen, A. Bhatnagar, M. Sillanpää, A review on modification methods to cellulose-based adsorbents to improve adsorption capacity. *Water Res.* **91**, 156–173 (2016).

85. X. Yu, S. Tong, M. Ge, L. Wu, J. Zuo, C. Cao, W. Song, Adsorption of heavy metal ions from aqueous solution by carboxylated cellulose nanocrystals. *J. Environ. Sci.* **25**, 933–943 (2013).

86. S. Hokkanen, E. Repo, M. Sillanpää, Removal of heavy metals from aqueous solutions by succinic anhydride modified mercerized nanocellulose. *Chem. Eng. J.* **223**, 40–47 (2013).

87. N. Isobe, X. Chen, U.-J. Kim, S. Kimura, M. Wada, T. Saito, A. Isogai, TEMPO-oxidized cellulose hydrogel as a high-capacity and reusable heavy metal ion adsorbent. *J. Hazard. Mater.* **260**, 195–201 (2013).

88. M. Hirota, N. Tamura, T. Saito, A. Isogai, Surface carboxylation of porous regenerated cellulose beads by 4-acetamide-TEMPO/NaClO/NaClO₂ system. *Cellulose* **16**, 841–851 (2009).

89. Y.-H. Li, S. Wang, J. Wei, X. Zhang, C. Xu, Z. Luan, D. Wu, B. Wei, Lead adsorption on carbon nanotubes. *Chem. Phys. Lett.* **357**, 263–266 (2002).

90. N. A. Kabbashi, M. A. Atieh, A. Al-Mamun, M. E. S. Mirghami, M. D. Z. Alam, N. Yahya, Kinetic adsorption of application of carbon nanotubes for Pb(II) removal from aqueous solution. *J. Environ. Sci.* **21**, 539–544 (2009).

91. Y.-H. Li, S. Wang, Z. Luan, J. Ding, C. Xu, D. Wu, Adsorption of cadmium(II) from aqueous solution by surface oxidized carbon nanotubes. *Carbon* **41**, 1057–1062 (2003).

92. Y.-H. Li, Z. Di, J. Ding, D. Wu, Z. Luan, Y. Zhu, Adsorption thermodynamic, kinetic and desorption studies of Pb²⁺ on carbon nanotubes. *Water Res.* **39**, 605–609 (2005).

93. P. Liang, Y. Liu, L. Guo, J. Zeng, H. Lu, Multiwalled carbon nanotubes as solid-phase extraction adsorbent for the preconcentration of trace metal ions and their determination by inductively coupled plasma atomic emission spectrometry. *J. Anal. At. Spectrom.* **19**, 1489–1492 (2004).

94. Y.-H. Li, J. Ding, Z. Luan, Z. Di, Y. Zhu, C. Xu, D. Wu, B. Wei, Competitive adsorption of Pb²⁺, Cu²⁺ and Cd²⁺ ions from aqueous solutions by multiwalled carbon nanotubes. *Carbon* **41**, 2787–2792 (2003).

95. C. Chen, X. Wang, Adsorption of Ni(II) from aqueous solution using oxidized multiwall carbon nanotubes. *Ind. Eng. Chem. Res.* **45**, 9144–9149 (2006).

96. C. Lu, C. Liu, Removal of nickel(II) from aqueous solution by carbon nanotubes. *J. Chem. Technol. Biotechnol.* **81**, 1932–1940 (2006).

97. C. Lu, H. Chiu, Adsorption of zinc(II) from water with purified carbon nanotubes. *Chem. Eng. Sci.* **61**, 1138–1145 (2006).

98. C. Chen, J. Hu, D. Shao, J. Li, X. Wang, Adsorption behavior of multiwall carbon nanotube/iron oxide magnetic composites for Ni(II) and Sr(II). *J. Hazard. Mater.* **164**, 923–928 (2009).

99. H. Wang, A. Zhou, F. Peng, H. Yu, J. Yang, Mechanism study on adsorption of acidified multiwalled carbon nanotubes to Pb(II). *J. Colloid Interface Sci.* **316**, 277–283 (2007).

100. G. Zhao, J. Li, X. Ren, C. Chen, X. Wang, Few-layered graphene oxide nanosheets as superior sorbents for heavy metal ion pollution management. *Environ. Sci. Technol.* **45**, 10454–10462 (2011).

101. X.-J. Hu, Y.-G. Liu, H. Wang, A.-W. Chen, G.-M. Zeng, S.-M. Liu, Y.-M. Guo, X. Hu, T.-T. Li, Y.-Q. Wang, L. Zhou, S.-H. Liu, Removal of Cu(II) ions from aqueous solution using sulfonated magnetic graphene oxide composite. *Sep. Purif. Technol.* **108**, 189–195 (2013).